

Optically thick winds of very massive stars suppress intermediate-mass black hole formation

Stefano Torniamenti^{1,2},                                                               <img alt="ID icon" data-b

is triggered or enhanced by stellar collisions during the earliest stellar phases (Portegies Zwart et al. 1999; Mapelli 2016). The possibility that VMSs form IMBHs, however, strongly depends on the amount of mass they lose during their life (Vink 2018).

At solar metallicity, VMSs can lose a large fraction of their initial mass already during the main sequence, and leave relatively low-mass compact objects ($< 30 M_{\odot}$, Belczynski et al. 2010; Mapelli et al. 2013; Romagnolo et al. 2024). At low metallicity, these stars could preserve enough mass to enter the pair-instability regime (Spera & Mapelli 2017; Renzo et al. 2020). Namely, stars developing He cores in the $64\text{--}135 M_{\odot}$ range at the end of carbon burning eventually explode as (pair-instability) supernovae leaving no compact remnant (Heger & Woosley 2002; Woosley et al. 2007; Yungelson et al. 2008), whereas stars that develop even more massive He cores efficiently undergo photodisintegration and possibly collapse into IMBHs (Spera & Mapelli 2017). Also, the retention of the envelope can trigger a dredge-up phase during the core helium-burning phase, remove mass from the stellar core and, in turn, prevent pair-production episodes (Costa et al. 2021).

Most current models predict that VMSs can form IMBHs up to metallicities $Z \lesssim 0.014$ (see, e.g., Costa et al. 2025), where stellar winds become strong enough to prevent the formation of stellar cores with $> 100 M_{\odot}$. Recently, Sabhahit et al. (2022, 2023, hereafter S22; S23) introduced a new model for stellar winds in VMSs based on the concept of transition mass loss (Vink et al. 2011; Vink & Gräfener 2012) to account for the transition from optically thin winds of O-type stars to the optically thick wind regime. This predicts enhanced mass-loss rates ($\dot{M} \gtrsim 10^{-4} M_{\odot} \text{ yr}^{-1}$) already during the main sequence, when the star is radiation-pressure dominated – i.e., when its luminosity is very close to or even above the Eddington value. In this case, the wind mass-loss rate is strong enough to reduce the core mass (S23). This improved wind implementation has proved to naturally account for the narrow range of observed VMS temperatures in the Galaxy and the LMC (S22). Also, it heavily suppresses the occurrence of pair instability due to lower core masses. In a recent work, we estimate that this new wind formalism can naturally yield rates of pair instability supernovae consistent with observations (Simonato et al. 2025). Another consequence we may naturally expect is the suppression of IMBH production from VMSs in the regime where optically thick winds become effective.

Here, we investigate the formation of IMBHs from VMSs. We account for optically thick winds to assess how different metallicities and mass-loss rates affect the formation of these objects. To this purpose, we have run an extensive set of VMS models with `MESA` (Paxton et al. 2011, 2018) to explore the impact of stellar winds on the mass of the VMS cores and the resulting BH masses. We find that IMBH formation is strongly suppressed by our optically thick wind model, even at the metallicity of the LMC.

This paper is organized as follows. In Sec. 2 we introduce our models for stars and stellar winds. In Sec. 3, we show the BH mass distributions from single and binary stars in presence of optically thick winds. In Sect. 4 we discuss the possible impact of rotation and core overshooting. Finally we summarize our results and conclusion in Sec. 5.

2. Methods

We model the evolution of VMSs with the hydro-static stellar evolution code `MESA` (version r12115; Paxton et al. 2011, 2013,

2015, 2018, 2019; Jermyn et al. 2023) adopting the radiation-driven wind models by S23. First, we evolve VMSs until the last phases before core collapse. Then, we use the population-synthesis code `SEVN` (Spera et al. 2019; Mapelli et al. 2020; Iorio et al. 2023) to explore the BH mass distribution of single and binary VMSs with different wind models and to study a population of massive binary stars. In the following, we introduce our initial conditions and model parameters.

2.1. VMS models with `MESA`

We adopt the same initial set-up as Simonato et al. (2025), based on the wind mass-loss scheme by S22 and S23¹. This wind model is based on the concept of transition mass loss introduced by Vink & Gräfener (2012): the transition from optically thin to optically thick winds takes place when the Eddington ratio of the star (Γ_{Edd}) exceeds the ratio at the transition point $\Gamma_{\text{Edd,tr}}$. At each iteration, we calculate the mass-loss rate \dot{M}_{Vink} , the escape velocity v_{esc} and the terminal speed v_{∞} from the stellar luminosity as described in S23. We use these quantities to calculate the wind efficiency parameter, which determines when the switch occurs:

$$\eta_{\text{Vink}}(L) \equiv \frac{\dot{M}_{\text{Vink}} v_{\infty}}{L/c} = \frac{\eta}{\tau_{F,s}} \left(\frac{v_{\infty}}{v_{\text{esc}}} \right) = 0.75 \left(1 + \frac{v_{\text{esc}}^2}{v_{\infty}^2}(L) \right)^{-1}, \quad (1)$$

where $\tau_{F,s}$ is the the flux-weighted mean optical depth at the sonic point. In the optically thick regime, the wind mass-loss follows Vink et al. (2011):

$$\dot{M} = \dot{M}_{\text{tr}} \left(\frac{L}{L_{\text{tr}}} \right)^{4.77} \left(\frac{M}{M_{\text{tr}}} \right)^{-3.99}, \quad (2)$$

where \dot{M}_{tr} , L_{tr} and M_{tr} are the mass-loss rate, the luminosity, and the mass at the transition point, respectively. During the main sequence, we use Eq. 2 to describe the wind mass-loss in the optically thick regime. Otherwise, we refer to Vink et al. (2001). In the core He-burning phase, we use Eq. 2 for temperatures between $4 \times 10^3 \text{ K}$ and 10^5 K , while for $T < 4 \times 10^3 \text{ K}$, we use the formalism by de Jager et al. (1988). For $T > 10^5 \text{ K}$ and central hydrogen mass fraction $X_{\text{C}} < 0.01$, we adopt the Wolf-Rayet mass-loss by Sander & Vink (2020).

We model convective mixing with the mixing length theory (Cox & Giuli 1968), adopting a constant mixing-length ratio $\alpha_{\text{MLT}} = 1.5$. We determine the convective boundaries by applying the Ledoux criterion (Ledoux 1947). We use the semi-convective diffusion parameter $\alpha_{\text{SC}} = 1$. We choose the exponential overshooting formalism by Herwig (2000), with efficiency parameter $f_{\text{ov}} = 0.03$, to describe this process above the convective regions.

Finally, we activate the `co_burn` net (parameter `auto_extend_net = true`) after the main sequence to have a complete and extended network for C- and O-burning and α -chains. Following Simonato et al. (2025), we define the core radius of each element as the radius inside which the fraction of the lighter element below $f_X = 10^{-4}$. For example, the helium (carbon) core radius is the radius inside which the mass fraction of H (${}^4\text{He}$) drops below $f_X = 10^{-4}$ ($f_Y = 10^{-4}$). Our definition is the same as the MIST libraries, and yields an accurate description of the core boundary (Paxton et al. 2011, 2013, 2015; Dotter 2016; Choi et al. 2016).

¹ The `MESA` inlists and `run_star_extras` files by Sabhahit et al. (2023) are publicly available at this link.

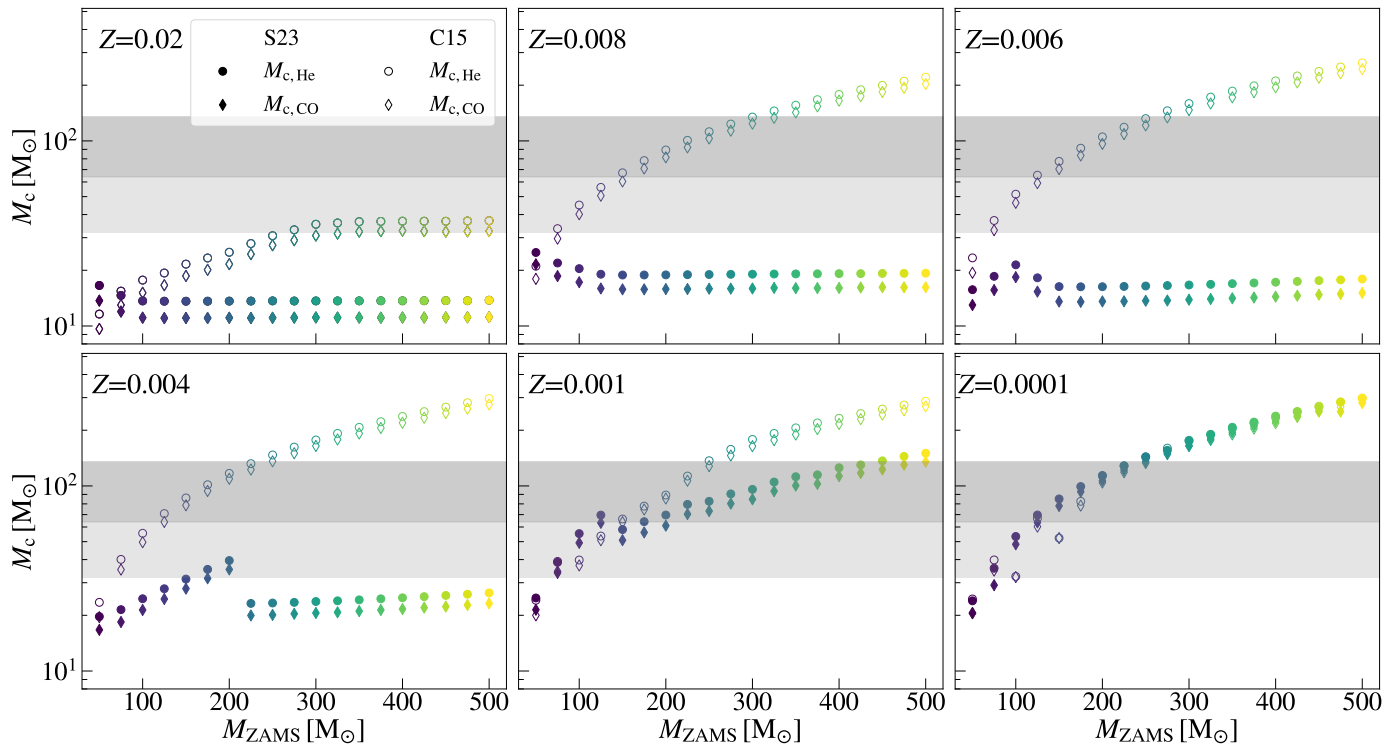


Fig. 1. Masses of the He (circles) and CO cores (diamonds) for the wind model from S23 (full markers) and C15 (void markers). The dark (light) gray shaded areas represent the regime for (pulsational) pair-instability supernovae.

2.2. Initial conditions and stopping criteria

We consider a grid of VMS models with masses from 50 to 500 M_{\odot} , by intervals of 25 M_{\odot} . We consider 14 metallicities from $Z = 10^{-4}$ to $Z = 0.02$. The initial He mass fraction is $Y = Y_{\text{prim}} + Z \Delta Y / \Delta Z$, with $Y_{\text{prim}} = 0.24$ the primordial He abundance and $\Delta Y / \Delta Z$ is parametrized so that we range from a primordial ($Y = 0.24$, $Z = 0$) to nearly a solar abundance ($Y = 0.28$, $Z = 0.02$, [Pols et al. 1998](#))². Finally, we calculate the H mass fraction as $X = 1 - Y - Z$. We consider only non-rotating stellar models.

We evolve the MESA models until the star exceeds a central temperature $\log T_c / \text{K} = 9.55$, corresponding to the very last stages before core collapse, or it undergoes (pulsational) pair-instability. In the latter case, the creation of electron-positron pairs removes thermal pressure from the gas, possibly triggering a state of global dynamical instability. Because we use the hydro-static integrator of MESA, we cannot integrate the models until (pulsational) pair instability kicks in, but we verify a posteriori the global stability of the star. Specifically, we calculate the first adiabatic exponent Γ_1 (e.g., see also [Marchant et al. 2019](#); [Farmer et al. 2019, 2020](#); [Costa et al. 2021](#)), properly weighted and integrated over the mass domain ([Stothers 1999](#)):

$$\langle \Gamma_1 \rangle = \frac{\int_0^M \frac{P}{\rho} \Gamma_1 dm}{\int_0^M \frac{P}{\rho} dm}. \quad (3)$$

Here, P is the pressure, ρ is the density and the integral is calculate up to the surface of the star. If a star enters a regime $\langle \Gamma_1 \rangle < 4/3 + 0.01$, we label it as pair-instability and no longer integrate its evolution.

² Here, we refer to the traditionally considered value for solar metallicity $Z = 0.02$ ([Grevesse & Sauval 1998](#); but see, e.g., [Magg et al. 2022](#) for more recent estimates).

2.3. BH masses

If the star enters the (pulsational) pair-instability regime, we calculate the final BH mass with the fitting formulas from [Mapelli et al. \(2020\)](#), based on the models by [Woosley \(2017\)](#). In this model, a star undergoes a pulsational pair-instability supernova if the He core has a final mass in the range $32 M_{\odot} \leq M_{\text{He,f}} < 64 M_{\odot}$. The mass of the BH is therefore estimated as

$$M_{\text{BH}} = \alpha_P M_{\text{CCSN}}, \quad (4)$$

where M_{CCSN} is the expected BH mass after a core-collapse supernova, based on the fitting formulas by [Fryer et al. \(2012\)](#), and α_P depends on the mass of He-core and on the ratio between the He-core mass and the total mass in the pre-supernova stage.

If $64 M_{\odot} \leq M_{\text{He,f}} \leq 135 M_{\odot}$, instead, the star undergoes a pair-instability supernova, leaving no compact remnant. If the core mass exceeds $135 M_{\odot}$, pair instability triggers photodisintegration and the star directly collapses into a BH, leaving a compact remnant with M_{BH} equal to the total mass of the star.

Mass ejection can also occur in stars that undergo a failed supernova because of the shock triggered by instantaneous neutrino loss ([Lovegrove & Woosley 2013](#); [Fernández et al. 2018](#)). The ejected mass depends on the ejected energy and the compactness of the star ([Fernández et al. 2018](#)). In particular, the ejected energy depends on the core compactness, $\xi_{2.5}$ ([O'Connor & Ott 2011](#); [Burrows & Vartanyan 2021](#); [Burrows et al. 2024](#)). Also, the ejected mass decreases with the stellar envelope compactness, $\xi_{\text{env}} = M_{*}/R_{*}$, where R_{*} is the total radius of the star. The ejected mass depends on ξ_{env} ([Fernández et al. 2018](#)), and ranges from $M_{\text{ej}} \sim 10 M_{\odot}$ for red supergiant stars ($\xi_{\text{env}} \sim 10^{-2}$) to $M_{\text{ej}} \lesssim 10^{-3} M_{\odot}$ if the star dies as a Wolf-Rayet object ($\xi_{\text{env}} \sim 10$).

Following [Costa et al. \(2022a\)](#), we estimate the BH mass for the stars that do not undergo a (pulsational) pair instability

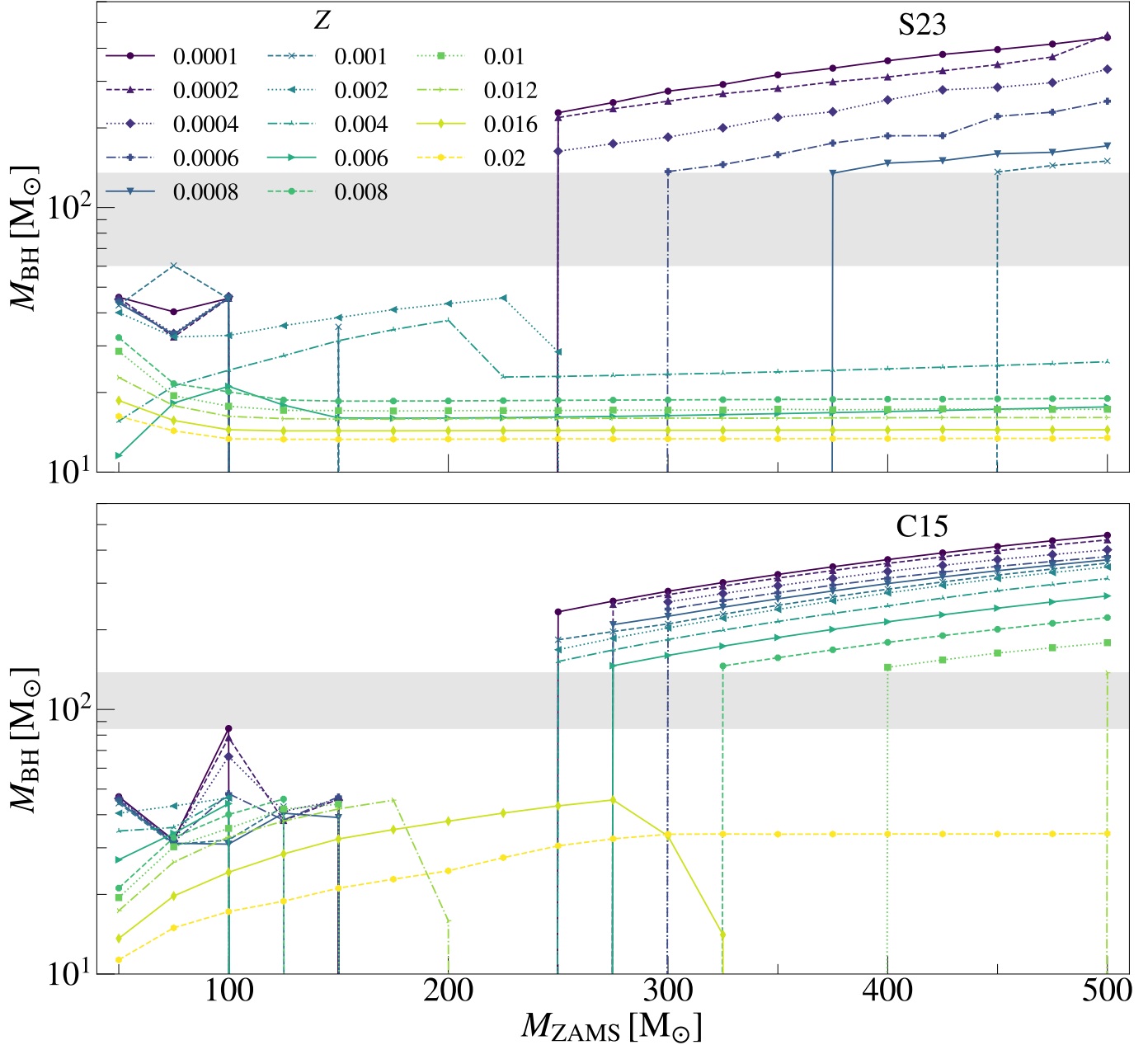


Fig. 2. Final BH mass as a function of M_{ZAMS} for different metallicities Z , for the S23 (upper) and C15 (lower) wind mass-loss prescription. The grey shaded area shows the resulting pair-instability mass gap for the two wind models.

supernova as:

$$M_{\text{BH}} = M_* - \delta M_{\text{G}} - M_{\text{ej}}, \quad (5)$$

where M_* is the final stellar mass, δM_{G} is the instantaneous gravitational mass loss, and M_{ej} is the mass induced by neutrino-driven shocks in a failed supernova. Here, we assume $\delta M_{\text{G}} = 0.3 M_{\odot}$ (Fernández et al. 2018; Costa et al. 2025), which typically yields a corresponding ejected energy between 10^{47} and 5×10^{47} erg. We thus calculate M_{ej} as the mass of the star with a binding energy less than 3×10^{47} erg.

2.4. Population-synthesis with SEVN

We explore the effect of optically thick winds on the mass spectrum of BHs, BBHs and BBH mergers using the population-

synthesis code SEVN (Spera & Mapelli 2017; Spera et al. 2019; Mapelli et al. 2020; Iorio et al. 2023)³. SEVN interpolates pre-computed stellar tracks to evolve single and binary stars. Also, it incorporates semi-analytic formulas for processes like binary mass transfer, tides, supernova explosion, and gravitational-wave decay. We refer to Iorio et al. (2023) for a complete description of the code.

We generate new evolutionary tables for stars with mass $M_{\star} \geq 50 M_{\odot}$ from the aforementioned VMS models with MESA. We then evolve single and binary stars with primary mass in this mass range. For binary stars, we use the stellar tables from PARSEC (Bressan et al. 2012; Chen et al. 2015; Costa et al. 2019a,b;

³ We used version 2.10.1 of SEVN, updated to commit c9dc8e457. SEVN is publicly available here.

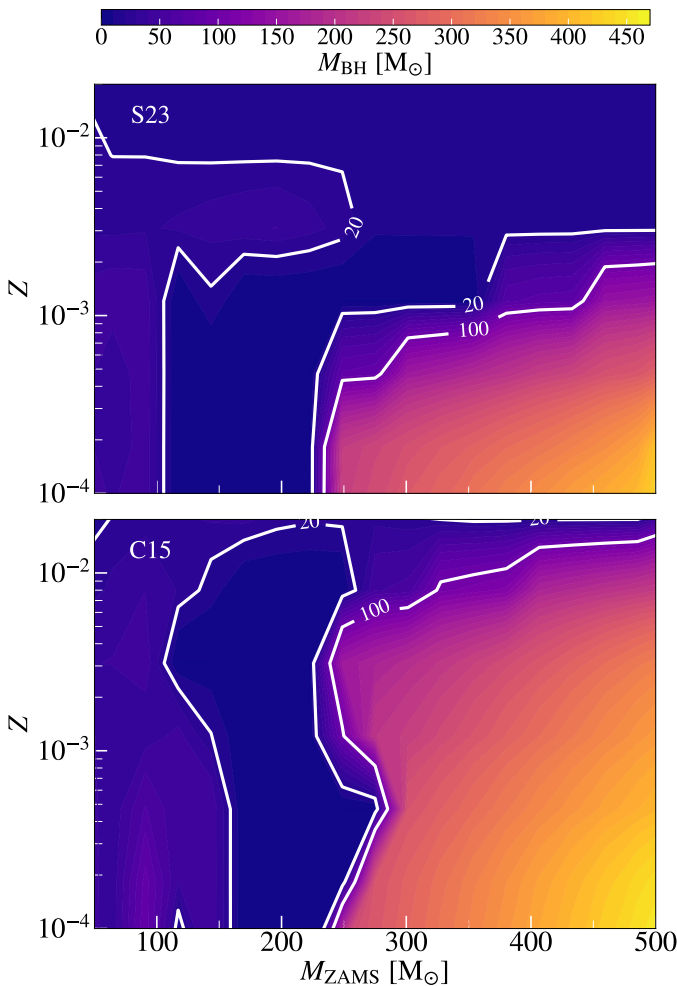


Fig. 3. Contour plot showing the final BH mass as a function of M_{ZAMS} and Z , for the **S23** (upper panel) and the **C15** (lower panel) models. The white contours highlight the levels at $20 M_{\odot}$ and $100 M_{\odot}$.

[Nguyen et al. 2022](#); [Costa et al. 2025](#)) to account for the evolution of secondary stars with mass $M_{\star} < 50 M_{\odot}$.

When two stars collide, we use the standard formalism of SEVN as described by [Iorio et al. \(2023\)](#). Specifically, we assume that the collision product retains the total mass of the two stars. The CO and He core masses of the collision product are the sum of the CO and He core masses of the two colliding stars. Finally, the collision product inherits the phase and percentage of life of the most evolved progenitor star. Hence, our models likely overestimate the total mass of the collision product and underestimate mixing. For a more self-consistent treatment of massive star collisions, see, e.g., [Costa et al. \(2022b\)](#) and [Ballone et al. \(2023\)](#).

We randomly draw the zero-age main sequence (ZAMS) primary star masses from a [Kroupa \(2001\)](#) initial mass function, with $M_{\text{ZAMS}} \in [50, 500]$. For binaries, we draw the secondary masses from the observation-based mass ratio distribution $\mathcal{F}(q) \propto q^{-0.1}$, with $q \in [0.1, 1]$ from [Sana et al. \(2012\)](#). We generate the initial orbital periods (P) and eccentricities (e) from the distributions by [Sana et al. \(2012\)](#): $\mathcal{F}(P) \propto P^{-0.55}$, with $P = \log_{10}(P/\text{days}) \in [0.15, 5.5]$ and $\mathcal{F}(e) \propto e^{-0.45}$, with $e \in [10^{-5}, e_{\text{max}}(P)]$, respectively. For a given orbital period, we set the upper limit of the eccentricity distribution $e_{\text{max}}(P)$ as $e_{\text{max}}(P) = 1 - [P/(2 \text{ days})]^{-2/3}$ ([Moe & Di Stefano 2017](#)).

We investigate eight different metallicities: $Z = 0.0001, 0.001, 0.002, 0.004, 0.006, 0.008, 0.01, 0.02$. For each metallicity, we generate 2×10^6 single and 1×10^7 binary systems. Our initial setup corresponds to the same as the fiducial model by [Iorio et al. \(2023\)](#).

To highlight the impact of stellar winds on the resulting BH mass distribution, we also perform a run with tables from the non-rotating PARSEC tracks presented by [Costa et al. \(2025\)](#)⁴. In this case, the adopted wind model is the same as described by [Chen et al. \(2015\)](#), hereafter **C15**. Specifically, the winds of massive O-type stars are modeled adopting the fitting formulas by [Vink et al. \(2000\)](#) and [Vink et al. \(2001\)](#), with the correction by [Gräfener & Hamann \(2008\)](#) to account for the effects of electron scattering. The mass-loss rate of an O-type star scales with the metallicity as $\dot{M} \propto Z^{\beta}$, where β depends on the Eddington ratio Γ_{Edd} : $\beta = 0.85$ for $\Gamma_{\text{Edd}} < 2/3$, $\beta = 2.45 - 2.4 \times \Gamma_{\text{Edd}}$ for $2/3 \leq \Gamma_{\text{Edd}} < 1$, and $\beta = 0.05$ for $\Gamma_{\text{Edd}} \geq 1$ ([Chen et al. 2015](#)). In this way, this formalism incorporates the dependence of mass loss on the Eddington ratio ([Gräfener & Hamann 2008](#); [Vink et al. 2011](#)). As for Wolf-Rayet (WR) stars, PARSEC adopts the prescriptions by [Sander et al. \(2019\)](#), which match the properties of Galactic WR stars of type C (WC) and type O (WO). We refer to [Costa et al. \(2025\)](#) for other details on these stellar tracks.

3. Results

3.1. Stellar cores

Figure 1 shows the final He and CO core masses for the **S23** and **C15** wind models. At low metallicity ($Z \leq 0.0001$), the two wind models predict the same monotonic increase of the He and CO core mass with M_{ZAMS} , because VMSs do not enter the optically thick wind regime. At these metallicities, the **C15** models generally yield slightly smaller cores, due to the different envelope undershooting and convection models ([Simonato et al. 2025](#)).

At higher metallicity, the two considered models **C15** and **S23** behave in a dramatically different way. According to **S23**, VMSs can enter the optically thick wind regime at $Z \geq 0.001$: such strong winds reduce the final total mass and core mass of VMSs, resulting in a flat or even decreasing trend of M_c with M_{ZAMS} . Hence, the **S23** model predicts smaller He and CO cores compared to **C15**, with a deep impact on the occurrence of (pulsational) pair instability.

The effect of optically thick winds in the **S23** model is twofold. On the one hand, the **S23** model results in a lower metallicity threshold below which VMSs can enter the (pulsational) pair instability regime: the threshold is $Z_{\text{th}} = 0.004$ and 0.01 for **S23** and **C15**, respectively. On the other hand, the formation of IMBHs via direct collapse is suppressed in the **S23** model for metallicity $Z \geq 0.001$, whereas the **C15** model allows the formation of IMBHs already at $Z \leq 0.008$ because of the lower wind mass-loss.

For example, at $Z = 0.001$ optically thick winds become effective for $M_{\text{ZAMS}} > 200 M_{\odot}$, when the stellar core is already well within the pair-instability regime. Mass loss prevents the He core mass from increasing above $135 M_{\odot}$. As a consequence, only VMSs with $M_{\text{ZAMS}} \gtrsim 450 M_{\odot}$ undergo direct collapse to IMBH in the **S23** model, whereas in **C15** IMBHs can form via direct collapse already at $M_{\text{ZAMS}} \sim 300 M_{\odot}$.

⁴ The PARSEC stellar tracks are publicly available at <http://stev.oapd.inaf.it/PARSEC/> ([Costa et al. 2025](#)).

For $Z = 0.004$, VMSs with $M_{\text{ZAMS}} \geq 200 M_{\odot}$ develop stellar winds that are strong enough to reduce the stellar core to $M_c < 30 M_{\odot}$, where even pulsational pair instability is inhibited.

For $Z \gtrsim 0.006$, VMSs in **S23** models undergo optically thick stellar winds throughout the mass range considered. This dramatically reduces final core masses, which display a weak dependence on M_{ZAMS} . For example, at $Z \sim 0.006$ the core mass for VMSs with $M_{\text{ZAMS}} > 400 M_{\odot}$ decreases from $\sim 200 M_{\odot}$ in the **C15** model to $\sim 20 M_{\odot}$ in **S23**.

3.2. BH masses

Figure 2 shows the final BH mass as a function of M_{ZAMS} for models **C15** and **S23**. The key difference between the two models is the metallicity threshold to form IMBHs; this is $Z_{\text{IMBH}} = 0.001$ and 0.012 for models **S23** and **C15**, respectively. In model **S23**, IMBH formation is suppressed at metallicity $Z > 0.001$ by the onset of optically thick winds. These strong winds erode the mass of the He core and prevent it from reaching the threshold $M_{\text{He}} \sim 135 M_{\odot}$, above which the star avoids to explode as a pair-instability supernova. Thus, even the most massive stars do not produce IMBHs in the **S23** model unless they have metallicity $Z \leq 0.001$. In contrast, the lower mass loss in model **C15** allows to grow larger cores and enables the formation of IMBHs up to $Z \sim 0.012$.

In absence of optically thick winds, the BH mass increases with M_{ZAMS} , up to the onset of (pulsational) pair instability, at $M_{\text{ZAMS}} \gtrsim 75 M_{\odot}$. For larger initial masses, the onset of direct collapse depends on metallicity. In the **C15** model, VMSs undergo (pulsational) pair instability up to $Z = 0.01$. At lower metallicities, all the models with $M_{\text{ZAMS}} > 400 M_{\odot}$ produce IMBHs, with masses ranging from $135 M_{\odot}$ to $450 M_{\odot}$. At $Z = 0.02$, instead, wind mass-loss is strong enough to prevent the onset of pair instability, leading to a maximum BH mass $M_{\text{BH}} \sim 30 M_{\odot}$.

In the **S23** model, the maximum metallicity at which IMBHs form is an order of magnitude lower ($Z = 0.001$) compared to **C15**. Below this threshold, the **S23** model produces IMBHs with masses in the same range as **C15**. At higher metallicities, the most massive BHs originate from stars with $M_{\text{ZAMS}} \sim 50 M_{\odot}$, while more massive stars deliver $M_{\text{BH}} \lesssim 15 M_{\odot}$. This happens because VMSs develop optically thick winds at an early stage, and spend all their lifetime with $\dot{M} > 10^{-5} M_{\odot} \text{ yr}^{-1}$. This results in a severe erosion of the core (Simonato et al. 2025; Boco et al. 2025). Overall, the **S23** models predict a pair-instability BH mass gap from $65 M_{\odot}$ to $135 M_{\odot}$.

Figure 3 shows the final BH mass as a function of the ZAMS mass and the metallicity for the **S23** model. The formation of IMBHs takes place only for VMSs with $M_{\text{ZAMS}} \gtrsim 250 M_{\odot}$ at $Z \leq 0.001$. Also, the formation of BHs with $M_{\text{BH}} > 20 M_{\odot}$ is suppressed for $Z > 0.01$ throughout the mass range.

3.3. BH mass function

3.3.1. BHs from single VMSs

Figure 4 shows the BH mass function from single VMSs assuming a Kroupa (Kroupa 2001) initial mass function. For $Z > 0.001$ optically thick winds strongly suppress the production of IMBHs from single stars. At $Z = 0.001$, the **S23** model still allows IMBH formation, but the efficient mass loss limits the maximum BH mass to $150 M_{\odot}$, compared to $350 M_{\odot}$ in the **C15** model. For higher metallicities, stellar winds progressively reduce the maximum BH mass in the **S23** model, down to $20 M_{\odot}$ at $Z = 0.02$.

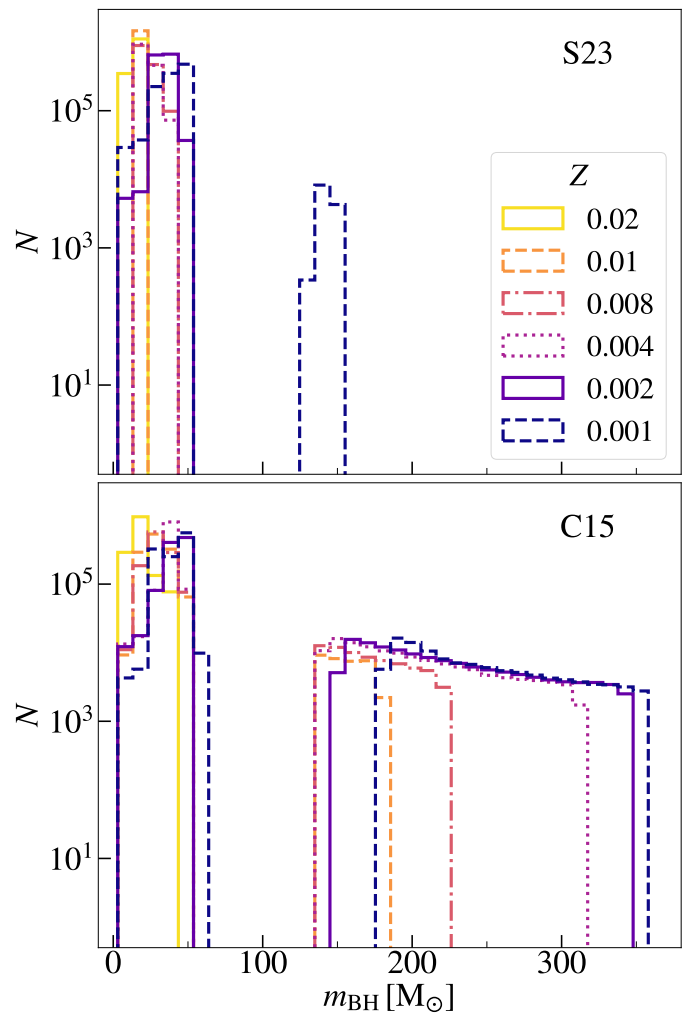


Fig. 4. BH mass distribution from single stars with $M_{\text{ZAMS}} > 50 M_{\odot}$, for the models adopting the **S23** (upper panel) and **C15** (lower panel) wind prescriptions and for different metallicities.

In the **C15** model, the formation of IMBHs takes place up to $Z = 0.01$, where the maximum BH mass is $\sim 180 M_{\odot}$ (see also Costa et al. 2025). At lower metallicities, the maximum IMBH mass reaches $\sim 400 M_{\odot}$, for ZAMS masses up to $M_{\text{ZAMS}} = 500 M_{\odot}$. In this model, IMBH formation from single VMSs is only suppressed at $Z = 0.02$, where BHs can form with a mass up to $33 M_{\odot}$.

3.3.2. BHs from VMS binaries

Figure 5 shows the primary BH masses from binaries with primary mass $M_{\text{ZAMS},1} > 50 M_{\odot}$, distributed according to a Kroupa (Kroupa 2001) mass function. We refer to Section 2.4 for more detail on the initial conditions. We display the mass distribution of both primary BHs in BBHs and single BHs from disrupted binaries. Star-star collisions dramatically extend the BH mass function to larger values compared to the single stellar-evolution case in Fig. 4.

The **C15** model predicts the formation of BHs as massive as $\gtrsim 700 M_{\odot}$ for $Z \leq 0.002$. Also, IMBHs up to $\sim 400 M_{\odot}$ can still form at $Z = 0.01$. In the **S23** model, instead, the formation of IMBHs is suppressed already at $Z = 0.004$, where they represent less than 0.2% of the total BH number, despite the occurrence of star-star collisions. In contrast, the percentage of IMBHs is 21%

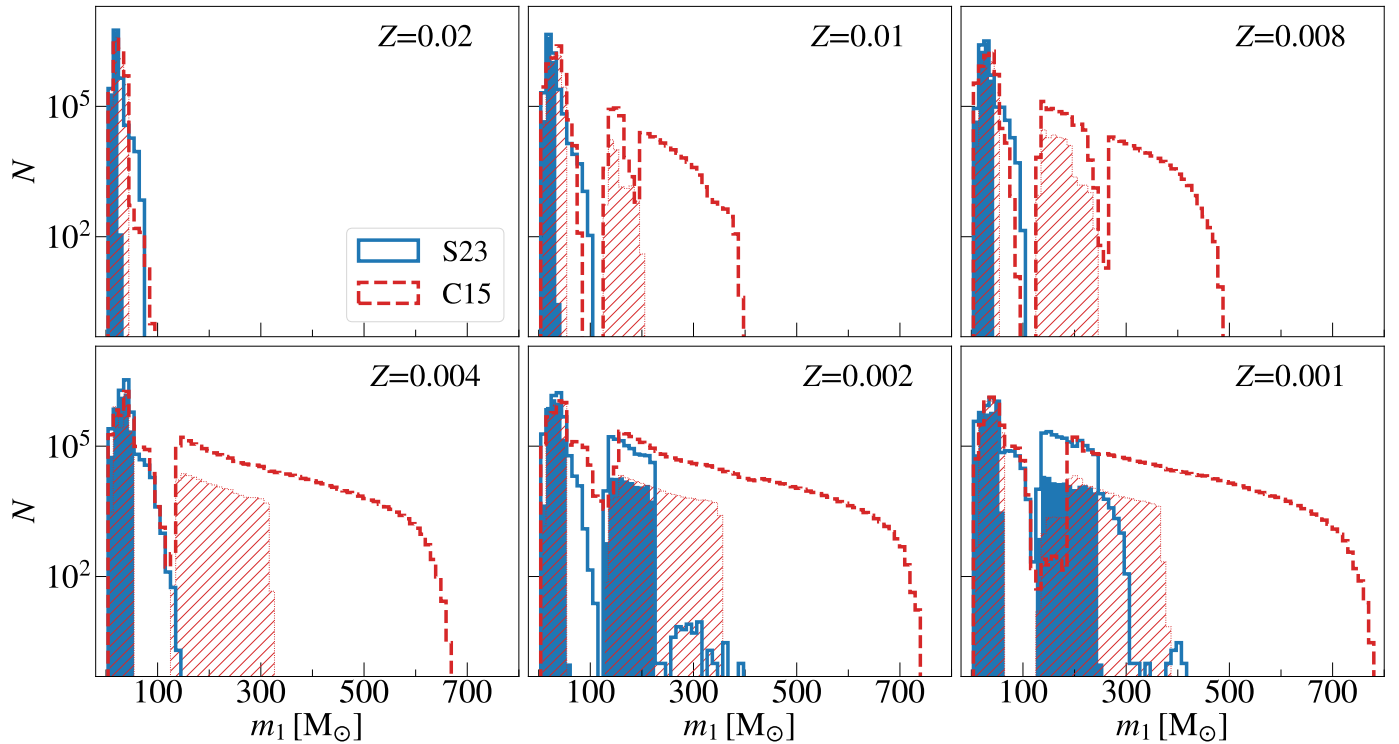


Fig. 5. BH mass distribution from binaries with $M_{\text{ZAMS},1} > 50 M_{\odot}$, for models adopting the S23 (blue, solid line, solid fill) and C15 (orange, dashed line, hatched area) wind prescriptions. The shaded (hatched) areas indicate the BHs in BBHs, while the empty histograms display the single BHs from disrupted binaries, including BHs that form from stellar collisions.

in the C15 model at $Z = 0.004$. We find that, in the metallicity range $Z = 0.004 - 0.008$, our distributions are consistent with those from Shepherd et al. (2025) when they consider the same wind prescription.

Primary BHs in BBHs also reach higher masses than BHs from single stellar evolution, due to mass accretion from the stellar companion. In the S23 model, IMBH formation in BBHs is possible for $Z \leq 0.002$, while for $Z = 0.004$, the maximum primary BH mass in BBHs decreases to $45 M_{\odot}$. At $Z = 0.02$, the BH mass function in the S23 model extends from $5 M_{\odot}$ to $20 M_{\odot}$.

BHs in BBHs display a pair-instability mass gap between $65 M_{\odot}$ and $135 M_{\odot}$ for both the C15 and the S23 models. In contrast, star-star collisions can produce BHs in this mass range, and fill the pair-instability mass gap with single BHs.

3.3.3. BBH mergers

Figures 6 and 7 show the primary and remnant mass distributions for BBHs that merge within a Hubble time. In the S23 model, no BBH merger has a primary mass $m_1 > 50 M_{\odot}$ for $Z > 0.002$. In the C15 case, IMBH mergers can occur up to a metallicity of $Z = 0.004$. In general, the BBH merger mass distribution displays a mild dependence on metallicity, with a peak at $\sim 10 M_{\odot}$.

The maximum merger remnant produced by these BBHs is usually two times as massive as the maximum primary BH mass. In presence of optically thick winds (model S23), the formation of IMBHs from BBH mergers is thus possible up to $Z = 0.002$, where $m_{\text{BH,max}} \sim 240 M_{\odot}$. At higher metallicities, the maximum BH remnant mass progressively decreases down to $35 M_{\odot}$ at $Z = 0.02$.

In the C15 models, the masses delivered by BBH mergers are larger, with the possibility of having IMBH remnants up to a metallicity of $Z = 0.006$.

3.3.4. Progenitors of GW231123 and GW190521

We qualitatively compare our models with the most massive BBH mergers detected by the LIGO-Virgo-KAGRA interferometers, namely GW231123 (The LIGO Scientific Collaboration et al. 2025c) and GW190521 (Abbott et al. 2020; Abbott et al. 2020). According to our S23 model, the progenitors of GW231123 should have had a metallicity $Z \leq 0.002$. The primary mass of GW190521 (Abbott et al. 2020; Abbott et al. 2020), instead, lies well within the mass gap predicted by both our C15 and S23 models. In a follow-up work, we will explore the dynamical formation of such mergers with our new S23 models (Torniamenti et al., in prep.).

4. Discussion

4.1. Impact of rotation and overshooting

In this work, we investigate the impact of a recent model accounting for optically thick winds (S23) on the formation of IMBHs from VMSs. We have considered non-rotating stellar models with a fixed overshooting parameter. However, both stellar rotation and core overshooting may have a relevant impact on the final BH mass. In a follow-up paper, we will include these additional parameters in detail. In the following, we briefly discuss their expected impact on our results.

Stellar rotation affects both the envelope and the core mass, leading to enhanced stellar-mass loss during the main sequence (Langer 1998, but see also Müller & Vink 2014), and triggering chemical mixing in the core (Sabahait et al. 2023). In the optically thin regime, rotation generally results in enhanced mass loss when the critical rotation is approached ($\Omega/\Omega_c > 0.4$). As a consequence, it can further quench the BH production at low

metallicity $Z < 0.01 Z_{\odot}$, where optically thick winds are not activated (Winch et al. 2024, 2025). Also, rotation can drive the transition to the optically-thick regime at lower initial masses (Sabahit et al. 2023; Boco et al. 2025). For VMS, this mainly affects the evolution at low Z , where the star can retain a large fraction of its angular momentum due to weaker mass loss. At high Z , wind mass loss can efficiently remove the angular momentum, leading to a minor impact from stellar rotation on the final BH mass.

Core overshooting also triggers chemical mixing, affecting the final core mass similarly to rotation (Sabahit et al. 2022). In the optically-thin regime, increasing the overshooting parameter leads to more massive cores, with larger values M_{BH} for the same M_{ZAMS} (Winch et al. 2024). For VMSs, optically thick winds already lead to the formation of a fully mixed star if the initial stellar mass is large enough ($M_{\text{ZAMS}} > 200 M_{\odot}$, Sabahit et al. 2022), while removing the stellar envelope. As a consequence, overshooting is not expected to play an important role on the final BH mass.

In summary, we expect overshooting and rotation to affect the relation between M_{ZAMS} and M_{BH} in the low-metallicity and low-mass end of the parameter space considered, where mass loss is driven by optically-thin winds. In such regimes, a larger overshooting parameter and a fast rotation may further reduce the maximum value of Z at which IMBHs are produced. When more vigorous stellar winds are present, VMS evolution is expected to mainly be driven by stellar mass loss, with a less relevant impact from these parameters.

4.2. Caveats of VMS population models

In our population-synthesis models, we have simply drawn primary stellar masses from a Kroupa IMF between 50 and $500 M_{\odot}$, corresponding to the extreme high-mass end of the mass function. In most star forming regions, the presence of stars in this mass range is dominated by stochastic effects or possibly by additional quenching effects (e.g., Weidner & Kroupa 2006). Thus, the conclusions of our population-synthesis simulations only apply to extreme star-forming regions, such as the R136 cluster in the LMC (Crowther et al. 2010; Bestenlehner et al. 2020), the super-star clusters in starburst galaxies (e.g., the Antennae galaxies, Whitmore & Schweizer 1995) and the high-redshift massive clusters recently discovered by the James Webb Space Telescope (Vanzella et al. 2023; Adamo et al. 2024; Mowla et al. 2024). Moreover, it is also possible that VMSs are the result of multiple stellar collisions in very dense star clusters (Portegies Zwart & McMillan 2002). In such case, population studies require dedicated N -body simulations (e.g., Di Carlo et al. 2021; Rantala et al. 2024).

5. Conclusions

We have investigated the impact of a new optically thick wind model (S23) on the formation of IMBHs in non-rotating isolated single and binary very massive stars (VMSs). The new model is supported by several observational constraints, such as the pair-instability supernova rate (Simonato et al. 2025) and the existence of single Wolf-Rayet stars at low metallicity (Boco et al. 2025). We have integrated the evolution of VMSs with MESA (Paxton et al. 2019) and have folded our new MESA tracks inside our binary population synthesis code sevn (Iorio et al. 2023).

We find that IMBH production is suppressed at intermediate metallicity ($Z \in [10^{-3}, 0.01]$), compared to less effective wind

models. According to our models, IMBHs cannot form from VMS collapse at the metallicity of the LMC ($Z \sim 0.008$) and possibly even the SMC ($Z \sim 0.0025$).

IMBHs might be able to form via stellar collisions at metallicity as high as $Z = 0.004$, but only under the very optimistic assumption that each collision triggers no mass loss. However, even with this assumption for stellar collisions, the occurrence fraction of IMBHs over the total number of BHs ($\lesssim 0.2\%$) is two orders of magnitude lower compared to models with less effective wind mass-loss.

BBH mergers can produce IMBH remnants at metallicity $Z \leq 0.002$. At higher metallicities, the enhanced mass-loss produces BBH mergers with primary mass $m_1 < 50 M_{\odot}$, making it impossible to form IMBHs from first-generation BH mergers.

The BH mass spectrum from single VMSs shows a pair-instability mass gap from $65 M_{\odot}$ to $135 M_{\odot}$. Such mass gap is still present in the mass distribution of BHs in BBHs and BBH mergers.

According to our S23 models, the progenitors of the most massive BBH observed by the LIGO-Virgo-KAGRA collaboration, GW231123 (The LIGO Scientific Collaboration et al. 2025c) must have had a metallicity $Z \leq 0.002$. In a follow-up study, we will explore the impact of star cluster dynamics on this result.

Acknowledgements. We thank the anonymous referee for their insightful comments and suggestions. We thank Gautham Sabahit and collaborators for sharing their MESA inlists (https://github.com/Apophis-1/VMS_Paper1, https://github.com/Apophis-1/VMS_Paper2). We thank Guglielmo Costa and Kendall Shepherd for useful comments and discussions. ST acknowledges financial support from the Alexander von Humboldt Foundation for the Humboldt Research Fellowship. ST, MM and GI acknowledge financial support from the European Research Council for the ERC Consolidator grant DEMOBLACK, under contract no. 770017. ST, MM and LB also acknowledge financial support from the German Excellence Strategy via the Heidelberg Cluster of Excellence (EXC 2181 - 390900948) STRUCTURES. GI acknowledges financial support from the La Caixa Foundation for the La Caixa Junior Leader fellowship 2024. GI also acknowledges financial support under the National Recovery and Resilience Plan (NRRP), Mission 4, Component 2, Investment 1.4, - Call for tender No. 3138 of 18/12/2021 of Italian Ministry of University and Research funded by the European Union – NextGenerationEU. EK and MM acknowledge support from the PRIN grant METE under contract No. 2020KB33TP. EK acknowledges financial support from the Fondazione Gini for the Gini grant. The authors acknowledge support by the state of Baden-Württemberg through bwHPC and the German Research Foundation (DFG) through grants INST 35/1597-1 FUGG and INST 35/1503-1 FUGG. We use the MESA software (<https://docs.mesastar.org/en/latest/>) version r12115; (Paxton et al. 2011, 2013, 2015, 2018, 2019). We use sevn (<https://gitlab.com/sevnCodes/sevn>) to generate our BBHs catalogs (Spera et al. 2019; Mapelli et al. 2020; Iorio et al. 2023), TRACKCRUNCHER (<https://gitlab.com/sevnCodes/trackcruncher>) (Iorio et al. 2023) to produce the tables for the interpolation. The PARSEC stellar tracks that we used for this work are publicly available at <http://stev.oapd.inaf.it/PARSEC/> (Costa et al. 2025). This research made use of NumPy (Harris et al. 2020), Pandas (The pandas development Team 2024), SciPy (Virtanen et al. 2020) and Matplotlib (Hunter 2007).

References

- Abbott, R., Abbott, T. D., Abraham, S., et al. 2020, ApJ, 900, L13
- Abbott, R., Abbott, T. D., Abraham, S., et al. 2020, Phys. Rev. Lett., 125, 101102
- Adamo, A., Bradley, L. D., Vanzella, E., et al. 2024, Nature, 632, 513
- Antonini, F., Gieles, M., Dosopoulou, F., & Chattpadhyay, D. 2023, MNRAS, 522, 466
- Antonini, F., Gieles, M., & Gualandris, A. 2019, MNRAS, 486, 5008
- Antonini, F., Romero-Shaw, I., Callister, T., et al. 2025, arXiv e-prints, arXiv:2509.04637

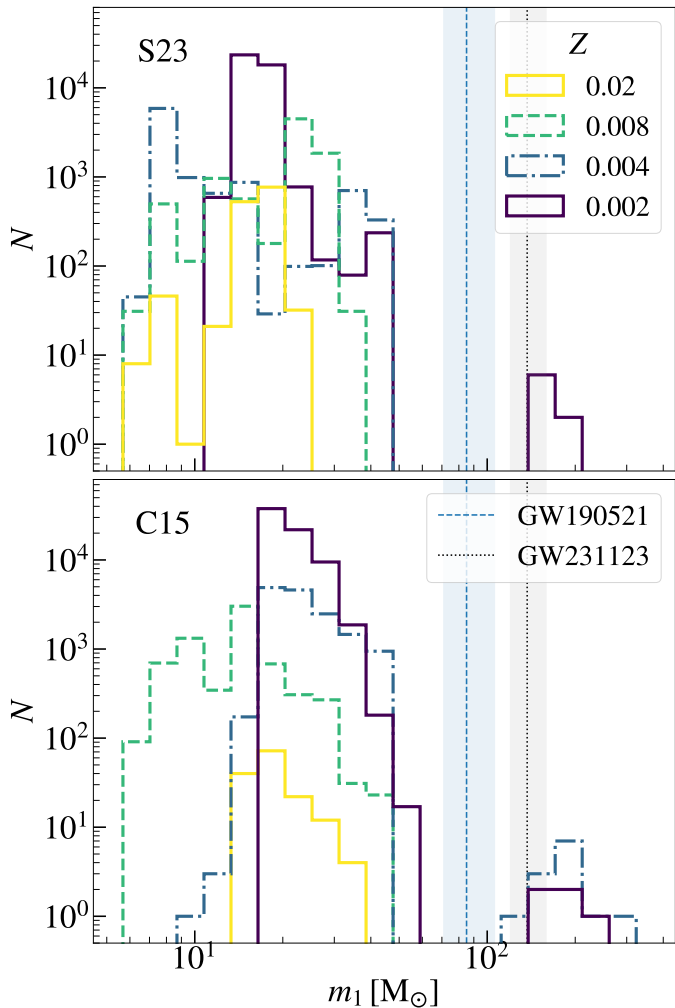


Fig. 6. Primary BH mass distribution in BBH mergers with $M_{\text{ZAMS},1} > 50 M_{\odot}$, for the S23 (upper) and C15 (lower) wind prescriptions, and for different metallicities. The blue dashed (black dotted) line displays the inferred value for GW190521 (GW231123), with the estimated uncertainty (shaded area).

Arca Sedda, M., Kamlah, A. W. H., Spurzem, R., et al. 2023, MNRAS, 526, 429
 Ballone, A., Costa, G., Mapelli, M., et al. 2023, MNRAS, 519, 5191
 Baumgardt, H., He, C., Sweet, S. M., et al. 2019, MNRAS, 488, 5340
 Belczynski, K., Bulik, T., Fryer, C. L., et al. 2010, ApJ, 714, 1217
 Belkus, H., Van Bever, J., & Vanbeveren, D. 2007, ApJ, 659, 1576
 Bestenlehner, J. M., Crowther, P. A., Caballero-Nieves, S. M., et al. 2020, MNRAS, 499, 1918
 Bestenlehner, J. M., Gräfener, G., Vink, J. S., et al. 2014, A&A, 570, A38
 Boco, L., Mapelli, M., Sander, A. A. C., et al. 2025, arXiv e-prints, arXiv:2507.00137
 Bressan, A., Marigo, P., Girardi, L., et al. 2012, MNRAS, 427, 127
 Burrows, A. & Vartanyan, D. 2021, Nature, 589, 29
 Burrows, A., Wang, T., & Vartanyan, D. 2024, ApJ, 964, L16
 Chen, Y., Bressan, A., Girardi, L., et al. 2015, MNRAS, 452, 1068

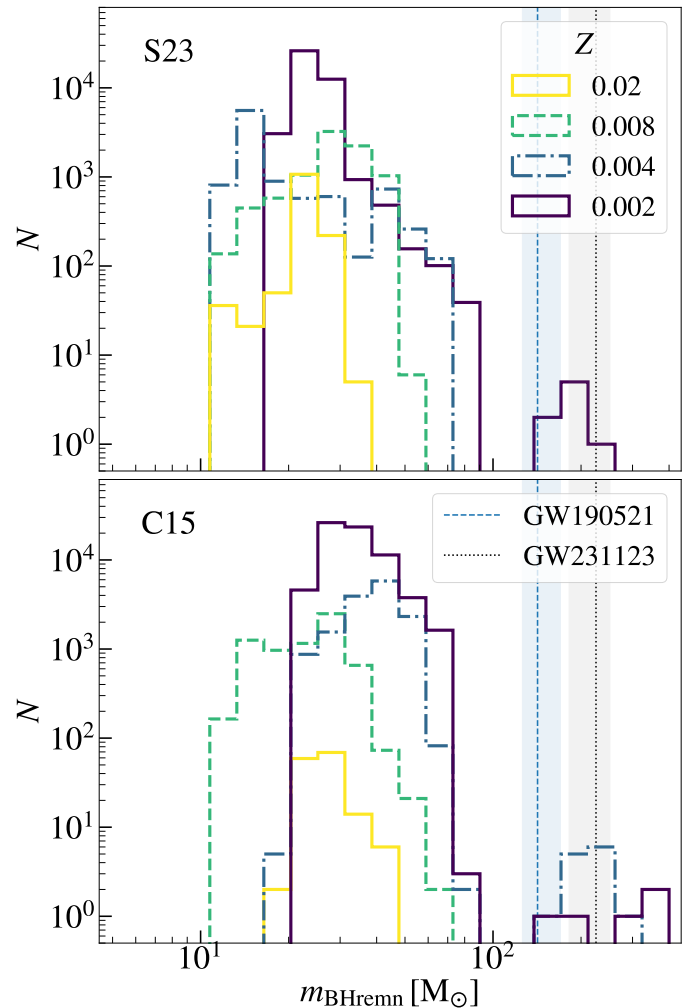


Fig. 7. Same as Fig. 6, but for the resulting BH remnant mass.

Choi, J., Dotter, A., Conroy, C., et al. 2016, ApJ, 823, 102
 Costa, G., Ballone, A., Mapelli, M., & Bressan, A. 2022a, MNRAS, 516, 1072
 Costa, G., Ballone, A., Mapelli, M., & Bressan, A. 2022b, MNRAS, 516, 1072
 Costa, G., Bressan, A., Mapelli, M., et al. 2021, MNRAS, 501, 4514
 Costa, G., Girardi, L., Bressan, A., et al. 2019a, A&A, 631, A128
 Costa, G., Girardi, L., Bressan, A., et al. 2019b, MNRAS, 485, 4641
 Costa, G., Shepherd, K. G., Bressan, A., et al. 2025, A&A, 694, A193
 Cox, J. P. & Giuli, R. T. 1968, Principles of stellar structure
 Crowther, P. A., Schnurr, O., Hirschi, R., et al. 2010, MNRAS, 408, 731
 de Jager, C., Nieuwenhuijden, H., & van der Hucht, K. A. 1988, Bulletin d'Information du Centre de Donnees Stellaires, 35, 141
 Di Carlo, U. N., Mapelli, M., Pasquato, M., et al. 2021, MNRAS, 507, 5132
 Dotter, A. 2016, ApJS, 222, 8
 Farmer, R., Renzo, M., de Mink, S. E., Fishbach, M., & Justham, S. 2020, ApJ, 902, L36
 Farmer, R., Renzo, M., de Mink, S. E., Marchant, P., & Justham, S. 2019, ApJ, 887, 53
 Fernández, R., Quataert, E., Kashiyama, K., & Coughlin, E. R. 2018, MNRAS, 476, 2366

Fishbach, M., Holz, D. E., & Farr, B. 2017, *ApJ*, 840, L24

Freitag, M., Gürkan, M. A., & Rasio, F. A. 2006a, *MNRAS*, 368, 141

Freitag, M., Rasio, F. A., & Baumgardt, H. 2006b, *MNRAS*, 368, 121

Fryer, C. L., Belczynski, K., Wiktorowicz, G., et al. 2012, *ApJ*, 749, 91

Gerosa, D. & Berti, E. 2017, *Phys. Rev. D*, 95, 124046

Gerosa, D. & Fishbach, M. 2021, *Nature Astronomy*, 5, 749

Gräfener, G. & Hamann, W. R. 2008, *A&A*, 482, 945

Greene, J. E., Strader, J., & Ho, L. C. 2020, *ARA&A*, 58, 257

Grevesse, N. & Sauval, A. J. 1998, *Space Sci. Rev.*, 85, 161

Häberle, M., Neumayer, N., Seth, A., et al. 2024, *Nature*, 631, 285

Harris, C. R., Millman, K. J., van der Walt, S. J., et al. 2020, *Nature*, 585, 357

Heger, A. & Woosley, S. E. 2002, *ApJ*, 567, 532

Herwig, F. 2000, *A&A*, 360, 952

Hunter, J. D. 2007, *Computing in Science and Engineering*, 9, 90

Iorio, G., Mapelli, M., Costa, G., et al. 2023, *MNRAS*, 524, 426

Jermyn, A. S., Bauer, E. B., Schwab, J., et al. 2023, *ApJS*, 265, 15

Kiroğlu, F., Kremer, K., Biscoveanu, S., González Prieto, E., & Rasio, F. A. 2025a, *ApJ*, 979, 237

Kiroğlu, F., Kremer, K., & Rasio, F. A. 2025b, *ApJ*, 994, L37

Kroupa, P. 2001, *MNRAS*, 322, 231

Langer, N. 1998, *A&A*, 329, 551

Ledoux, P. 1947, *ApJ*, 105, 305

Lovegrove, E. & Woosley, S. E. 2013, *ApJ*, 769, 109

Magg, E., Bergemann, M., Serenelli, A., et al. 2022, *A&A*, 661, A140

Mapelli, M. 2016, *MNRAS*, 459, 3432

Mapelli, M., Dall'Amico, M., Bouffanais, Y., et al. 2021, *MNRAS*, 505, 339

Mapelli, M., Spera, M., Montanari, E., et al. 2020, *ApJ*, 888, 76

Mapelli, M., Zampieri, L., Ripamonti, E., & Bressan, A. 2013, *MNRAS*, 429, 2298

Marchant, P., Renzo, M., Farmer, R., et al. 2019, *ApJ*, 882, 36

Martins, F., Hillier, D. J., Paumard, T., et al. 2008, *A&A*, 478, 219

Mezcua, M. 2017, *International Journal of Modern Physics D*, 26, 1730021

Miller-Jones, J. C. A., Wrobel, J. M., Sivakoff, G. R., et al. 2012, *ApJ*, 755, L1

Moe, M. & Di Stefano, R. 2017, *ApJS*, 230, 15

Mowla, L., Iyer, K., Asada, Y., et al. 2024, *Nature*, 636, 332

Müller, P. E. & Vink, J. S. 2014, *A&A*, 564, A57

Nguyen, C. T., Costa, G., Girardi, L., et al. 2022, *A&A*, 665, A126

O'Connor, E. & Ott, C. D. 2011, *ApJ*, 730, 70

Paxton, B., Bildsten, L., Dotter, A., et al. 2011, *ApJS*, 192, 3

Paxton, B., Cantiello, M., Arras, P., et al. 2013, *ApJS*, 208, 4

Paxton, B., Marchant, P., Schwab, J., et al. 2015, *ApJS*, 220, 15

Paxton, B., Schwab, J., Bauer, E. B., et al. 2018, *ApJS*, 234, 34

Paxton, B., Smolec, R., Schwab, J., et al. 2019, *ApJS*, 243, 10

Pols, O. R., Schröder, K.-P., Hurley, J. R., Tout, C. A., & Eggleton, P. P. 1998, *MNRAS*, 298, 525

Portegies Zwart, S. F., Makino, J., McMillan, S. L. W., & Hut, P. 1999, *A&A*, 348, 117

Portegies Zwart, S. F. & McMillan, S. L. W. 2002, *ApJ*, 576, 899

Rantala, A., Naab, T., & Lahén, N. 2024, *MNRAS*, 531, 3770

Renzo, M., Farmer, R. J., Justham, S., et al. 2020, *MNRAS*, 493, 4333

Rizzuto, F. P., Naab, T., Spurzem, R., et al. 2021, *MNRAS*, 501, 5257

Romagnolo, A., Gormaz-Matamala, A. C., & Belczynski, K. 2024, *ApJ*, 964, L23

Sabahhit, G. N., Vink, J. S., Higgins, E. R., & Sander, A. A. C. 2022, *MNRAS*, 514, 3736

Sabahhit, G. N., Vink, J. S., Sander, A. A. C., & Higgins, E. R. 2023, *MNRAS*, 524, 1529

Sana, H., de Mink, S. E., de Koter, A., et al. 2012, *Science*, 337, 444

Sander, A. A. C., Hamann, W. R., Todt, H., et al. 2019, *A&A*, 621, A92

Sander, A. A. C. & Vink, J. S. 2020, *MNRAS*, 499, 873

Shepherd, K. G., Costa, G., Ugolini, C., et al. 2025, *arXiv e-prints*, arXiv:2505.10206

Simonato, F., Torniamenti, S., Mapelli, M., et al. 2025, *arXiv e-prints*, arXiv:2505.07959

Spera, M. & Mapelli, M. 2017, *MNRAS*, 470, 4739

Spera, M., Mapelli, M., Giacobbo, N., et al. 2019, *MNRAS*, 485, 889

Stothers, R. B. 1999, *MNRAS*, 305, 365

The LIGO Scientific Collaboration, the Virgo Collaboration, & the KAGRA Collaboration. 2025a, *arXiv e-prints*, arXiv:2508.18083

The LIGO Scientific Collaboration, The Virgo Collaboration, & the KAGRA Collaboration. 2025b, *arXiv e-prints*, arXiv:2508.18082

The LIGO Scientific Collaboration, the Virgo Collaboration, the KAGRA Collaboration, et al. 2025c, *arXiv e-prints*, arXiv:2507.08219

The pandas development Team. 2024, *pandas-dev/pandas: Pandas*

Torniamenti, S., Mapelli, M., Périgois, C., et al. 2024, *A&A*, 688, A148

Torniamenti, S., Rastello, S., Mapelli, M., et al. 2022, *MNRAS*, 517, 2953

Tremou, E., Strader, J., Chomiuk, L., et al. 2018, *ApJ*, 862, 16

Vanbeveren, D., Belkus, H., Van Bever, J., & Mennekens, N. 2009, *Ap&SS*, 324, 271

Vanzella, E., Claeysens, A., Welch, B., et al. 2023, *ApJ*, 945, 53

Vink, J. S. 2018, *A&A*, 615, A119

Vink, J. S., de Koter, A., & Lamers, H. J. G. L. M. 2000, *A&A*, 362, 295

Vink, J. S., de Koter, A., & Lamers, H. J. G. L. M. 2001, *A&A*, 369, 574

Vink, J. S. & Gräfener, G. 2012, *ApJ*, 751, L34

Vink, J. S., Heger, A., Krumholz, M. R., et al. 2015, *Highlights of Astronomy*, 16, 51

Vink, J. S., Muijres, L. E., Anthonisse, B., et al. 2011, *A&A*, 531, A132

Virtanen, P., Gommers, R., Oliphant, T. E., et al. 2020, *Nature Methods*, 17, 261

Weidner, C. & Kroupa, P. 2006, *MNRAS*, 365, 1333

Whitmore, B. C. & Schweizer, F. 1995, *AJ*, 109, 960

Winch, E. R. J., Sabahhit, G. N., Vink, J. S., & Higgins, E. R. 2025, *MNRAS*, 540, 90

Winch, E. R. J., Vink, J. S., Higgins, E. R., & Sabahhit, G. N. 2024, *MNRAS*, 529, 2980

Woosley, S. E. 2017, *ApJ*, 836, 244

Woosley, S. E., Blinnikov, S., & Heger, A. 2007, *Nature*, 450, 390

Yungelson, L. R., van den Heuvel, E. P. J., Vink, J. S., Portegies Zwart, S. F., & de Koter, A. 2008, *A&A*, 477, 223